Modeling the physical layer of air-to-space optical communication networks using the modified multi-scale method

Helsdingen, Wieger; Den Breeje, Remco; Saathof, Rudolf

DOI
10.1364/JOCN.551182

Publication date
2025

Document Version
Final published version

Published in
Journal of Optical Communications and Networking

JOURNAL OF
Optical Communications
and Networking

Modeling the physical layer of air-to-space optical communication networks using the modified multi-scale method

Wieger Helsdingen,[1] Remco den Breeje,[2] and Rudolf Saathof[1,*]

[1]Space Systems Department of Aerospace Engineering Faculty, Delft University of Technology, Kluyverweg 1, Delft, 2629 HS, The Netherlands
[2]Airbus Netherlands, Mendelweg 30, Leiden, 2333 CS, The Netherlands
*R.Saathof@tudelft.nl

Received 11 December 2024; accepted 8 January 2025; published 11 February 2025

To support the development of free-space-optical (FSO) communication technologies, an end-to-end physical layer model of a satellite communication service was developed. This service involves physical processes spanning multiple time scales: hours (relative platform dynamics), minutes (link selection, atmospheric attenuation), milliseconds (atmospheric turbulence, platform disturbances), and nanoseconds (photon and bit transportation). The modified multi-scale method (MMM) was used to combine the physics of these processes and to model an end-to-end global FSO communication service between an airborne platform and a satellite constellation. The method provides a better understanding of physical interdependencies, allows performance analysis on multiple time scales, and enables valuable insight into where to optimize such a service. The results show realistic performance metrics when compared to other smaller-scale models and demonstrations. The MMM can be used as a mission performance indicator of an end-to-end satellite communication service.

https://doi.org/10.1364/JOCN.551182

1. INTRODUCTION

Free-space-optical (FSO) satellite communication enables data transfer with low latency, high security, and high bandwidth in an unlicensed spectrum [1]. Owing to these benefits, FSO communication services with satellite constellations can significantly improve global connectivity, bandwidth, and data security. Modeling such a satellite communication service will prove beneficial as it provides insight into the physics and performance of these large-scale missions. However, such models are complex and involve several physical processes that occur on different time scales. (1) Relative platform dynamics vary within hours and are dominated by the satellite's orbital period [2]. (2) A link selection process is required to initiate a link between a space-based terminal and an Earth-based terminal, occurring every 5–10 min for low-Earth-orbiting (LEO) constellations [3]. (3) Slow-atmospheric variations (cloud motion and attenuation) occur within minutes [4]. (4) Atmospheric turbulence and platform jitter (vibrations) typically occur in the region of 1–100 ms [5,6]. Finally, considering multi-Gbps capacity, (5) transportation and processing of photons and bits occur on a nanosecond time scale [7].

Many studies have been performed to simulate missions that include these processes. Most models focused specifically on atmospheric turbulence, attenuation, and platform vibrations [5,8–10] and some also included bit transportation processes [11–13]. Another focus was on network latency, where the routing of inter-satellite-links (ISLs) was modeled [14]. However, these models focused only on one or a few processes at a time. A more complete laser communication model was developed [11] that focused on a static link but neglected the platform dynamics. An end-to-end model was developed to simulate the latency and transmission performance of an optical constellation [15], which included many dominant physical processes. However, these models excluded essential performance drivers such as availability, quality, and capacity. Additionally, the different time scales, as well as the interdependencies between these time scales, have not yet been considered in these studies.

Therefore, in this paper, we propose the modified multi-scale method (MMM). It models all physical layer processes described above in their respective time scales and efficiently combines these to enable insight into the interdependencies of these processes. General applicability of the MMM was pursued by connecting system hardware parameters (input) to service performance drivers (output). Additionally, communication perturbations, which are typically analyzed on link level, were linked to the mission level. The MMM did not take into account coding and adaptive adjustment techniques. However, a modular integration approach was used to enable the addition of these features to the model. An aircraft-to-satellite

communication service was used as a case study. The MMM can also be extended to other types of communication services, including ISLs and ground-to-satellite links (GSLs). Here, we defined end-to-end as the simulation of the physical layer, from the transmission to the reception of the bits.

First, the problem and its physical processes were defined, and the mission drivers were derived in Section 2 to select the performance metrics that are the outputs of the model. Then Section 3 elaborates on the MMM design. Sub-models for each physical process were selected from the literature and modified where needed in Section 4. Then, the aircraft-to-satellite case study was used to demonstrate the results in Section 5. Finally, Section 6 concludes the study.

2. PROBLEM DESCRIPTION

The physical problem considered in this study encompassed a FSO communication service between an aircraft and a satellite constellation, as shown in Fig. 1. The processes in the physical layer were modeled along with the service performance drivers and constraints.

A. Physical Layer Processes

The physical problem spans various time scales in which the physical processes occur. The time scale of platform dynamics is driven by the aircraft trajectory and the satellite orbital period, which is approximately 90–120 min for LEO orbits [2]. The link selection process depends on the link duration, which typically ranges between 5–10 min for LEO satellites [3]. Acquisition, tracking, and pointing (ATP) processes typically take approximately 20–50 s, considering current industrial ATP standards [16]. Slow atmospheric effects are caused by clouds, molecules, and aerosols, which are dominated by atmospheric wind speeds varying within a time scale of minutes [7]. Atmospheric turbulence typically occurs within 1–50 ms [5]. Platform vibrations depend on the spectrum of the vehicle's mechanical vibrations, typically ranging between 1 ms and 100 ms. Other vibrational effects are considered much smaller and are neglected in this study. Finally, considering a multi-Gbps data rate, all physical processes involving transported bits and photons occur within a time scale of nanoseconds.

For clarity, all processes were divided into four levels: mission, link, channel, and bit. Processes at the mission and link levels, with a frequency lower than 1 Hz, are macroscopic. Processes at the channel and bit level, higher than 1 Hz, are microscopic. These two divisions were used to fit the processes in the MMM, which is further discussed in Section 3.

B. Performance Metrics and Constraints

To integrate the physical processes in Fig. 1, four metrics were identified that were deemed dominant in terms of the performance of a FSO satellite communication service. These are the availability, quality, capacity, and latency. Latency consists of propagation delay and node delay at the satellites [15]. This is primarily caused by inter-satellite-links in the backbone [14]. As we only modeled the uplink, we omitted latency in this study and selected availability, quality, and capacity as the performance metrics.

Availability was defined as the time fraction of successful communication between the aircraft and the satellites, thus indicating performance at mission level [17]. First, the active links were simulated, requiring a simulation of both aircraft and satellite trajectories as well as a link selection. These links were then tested for successful communication by setting a link margin threshold for the received power P_r. It was modeled at mission level and link level.

Quality describes the number of erroneously received bits against the total number of transmitted bits and was modeled using the bit error rate (BER) and the fractional fade time. Quality variations are owed to fading, which is predominantly caused by atmospheric turbulence and pointing jitter. Therefore, quality was modeled at the channel level. Owing to turbulence, this process is partly stochastic. Modeling the fading statistics of the received signal also allows for insight into the temporal behavior of the signal and can be used for sizing the link quality with the use of interleaving and coding schemes [18].

Capacity was defined here as the potential throughput that can be achieved through communication between the aerial platform and the constellation. Nielsen's law states an increasing global need for capacity [19] making it an essential driver of laser satellite communication services. It was modeled using the Shannon-Hartley theorem, as described on p. 111 of [20]. Furthermore, our model assumed a fixed data rate. The actual throughput was then modeled by removing erroneous bits and unavailable communication periods from the data rate.

The most dominant constraints concerning mission performance were identified and divided into three types, as listed in Table 1. These were used as input parameters for the model.

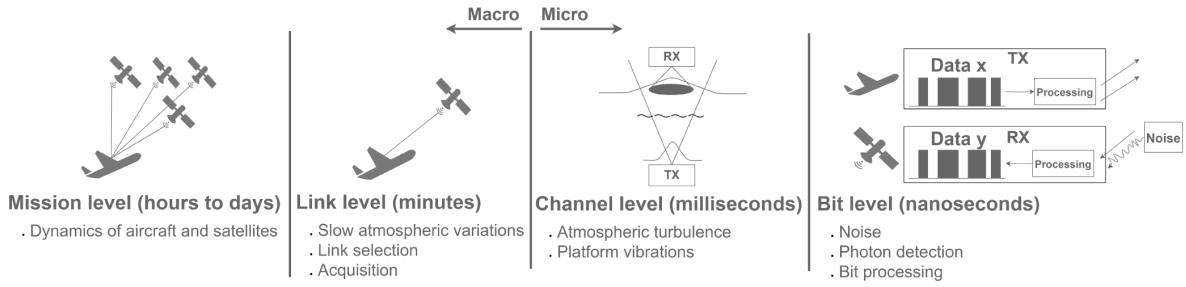

Fig. 1. Graphical overview of the physical problem. It is divided into four distinct scales based on the time scales at which all dominant physical processes occur.

Table 1. Model Constraints Used for Input

Constraint	Description
Hardware	Mechanical, electrical, and optical system characteristics of the transceiver terminals of both the aircraft and the satellites
Environment	Atmospheric properties (attenuation coefficient, background irradiance, and cloud transmission) and solar irradiance
Mission	Initial conditions of the aircraft and constellation to use for the propagation of their trajectories

C. Scope

The research scope was narrowed down to the physical layer as defined by the OSI model [21]. The philosophy of the MMM method can be applied to all kinds of communication services, including GSLs and ISLs. The current model is built to simulate air-to-space communication networks and modeled an uplink between the transmitting aircraft terminal and a sequence of receiving satellite terminals. As versatility was one of the main drivers for the MMM, all sub-models were modularly integrated, such that the current model can be extended to other use cases. For GSL networks, additional cloud cover and attenuation (models) need to be integrated. For ISLs, a more advanced routing model must be developed. Since we focused on the physical layer, coding and adaptive adjustment techniques were not implemented yet. As with the physical models, with the proper background knowledge, it should be relatively straightforward to implement this in the model. Furthermore, Shannon-Hartley was used to estimate the potential throughput, which is an overestimation of the actual available throughput. Finally, we assumed that the satellite constellation has a continuous internet connection with ground stations such that direct data transmission is possible after acquisition.

3. MODIFIED MULTI-SCALE METHOD

The proposed multi-scale method was based on a trade-off among four existing methods. To develop an efficient and accurate method that can be generally applied as a tool for FSO satellite communication analysis, four criteria were selected: speed, accuracy, versatility, and complexity. The methods were selected from the literature based on their usefulness for integration problems that deal with physical processes on multiple time scales. (1) The time-parallel compound wavelet matrix method (TPCWM) [22] effectively combined multiple time scales in parallel, but it was not deemed suitable for our problem because it requires first-order agreement between the coarse- and fine-scale solutions, which cannot be guaranteed in this case. (2) The coarse-grained Monte Carlo method (CGMCM) [23] used an inherently stochastic approach with Markov random fields. This made it efficient for fully stochastic processes, but it was less suitable for modeling the deterministic processes that are involved. (3) The heterogeneous multi-scale method (HMM) [24] used a generic method that can be applied to a wide variety of problems with measured accuracy. However, owing to a serial propagation, it lacked efficiency. (4) The sequential coupling method [25] was commonly used because it intuitively coupled a pre-computed microscopic state to the macroscopic state, such that they can be computed separately. However, in our case, it required a very high number of microscopic evaluations because of the many interdependencies between processes on the different time scales. Consequently this method lacked efficiency.

Based on this trade-off, we selected the HMM, which exhibited the best combination of accuracy, versatility, and complexity [24]. To further improve the efficiency of serial propagation, the time-parallel approach from the TPCWM was added. The proposed combination of the HMM and the TPCWM is called the modified multi-scale method (MMM). A graphical overview of this method is shown in Fig. 2.

In essence the MMM used sub-models to simulate each physical process and then reordered these in such a way that they could be combined on the multiple scales. First a macro-scale model was defined with mission and link level processes. This defined the inputs for the micro-scale, which is a description of the main disturbance processes that influence the communications performance. This communications performance was integrated in the macro-scale, which was then propagated to the aggregated service performance.

The macro-scale model propagated the macroscopic state $\boldsymbol{U}^{0,T}$ with time steps $\boldsymbol{T}_i$. This state contained the link margin P_r, the signal-to-noise ratio (SNR), and the BER. The macroscopic state required constraints described in Table 1 and the relative link geometry. The latter was modeled as the relative state vector $\boldsymbol{G}$, containing the slant range, the looking angles and their rates (elevation, azimuth, and zenith), and the slew rate (explained in more detail in Section 4.A). This state was iterated to $\boldsymbol{U}^{1,T}$ using the integrated microscopic information $\boldsymbol{D}^T$.

$\boldsymbol{D}^T$ comes from the micro-scale model, which propagated the microscopic state $\boldsymbol{u}_t^T$ (also containing P_r, the SNR, and the BER) with time steps $\boldsymbol{t}_{i,j}$. In this model, all micro-scale effects were modeled after which P_r, the SNR, and the BER were computed. Coding, modulation, and adaptive adjustment techniques can be implemented here. This state required constraints and local macroscopic information from the macro-scale. The method evaluated $\boldsymbol{N}$ micro-scale time steps for each macro-scale time step, leading to $\boldsymbol{M} \times \boldsymbol{N}$ evaluations in total.

The MMM was then applied to the problem described in Section 2, resulting in the functional diagram shown in Fig. 3. The blue blocks represent the physical layer processes. All recursions between the processes are omitted, and the functional flow between all sub-models is one-way. In reality, recursions exist between processes at various levels (black lines). For example, the link geometry directly determines the link budget. However, the link budget can also be used to optimize the link geometry by choosing an optimal link sequence. For this reason, our method serves as a lower-bound performance indicator. However, the MMM was selected as it is well suited to extend to this by adding cross-links between the processes and thus adding recursion. Furthermore, considering versatility as one of the main criteria of the model, all sub-models were aimed at being mutually exclusive and collectively exhaustive.

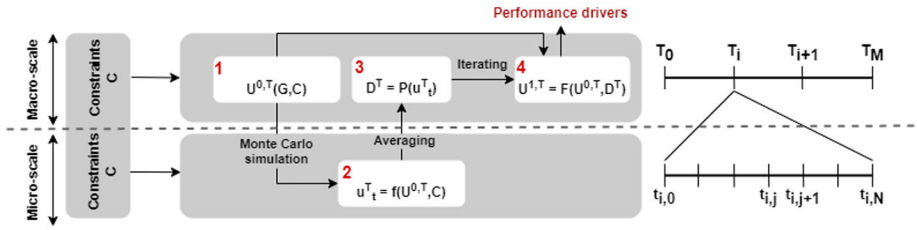

Fig. 2. Overview of the model philosophy of the MMM, containing four steps (indicated in red). The macro-scale (top) was simulated with time steps $\boldsymbol{T}_i$, resulting in the macroscopic state $\boldsymbol{U}^T$. At each macro time step, the micro-scale (bottom) was simulated in parallel with time steps $\boldsymbol{t}_{i,j}$, resulting in the microscopic state $\boldsymbol{u}_t^T$.

4. PHYSICAL MODELING

For each physical process in Fig. 3, we selected a model from the literature, or modified it if necessary, which is as simple as possible, while retaining sufficient accuracy. This was in line with the accuracy, efficiency, and complexity criteria for the MMM.

A. Mission Level

At this level, a model was created to simulate the satellite and aircraft trajectories. From this the relative geometries between the satellites and aircraft were computed and obtained in a relative state vector $\boldsymbol{G}$. Then a sequence of links was defined between the aircraft and the satellites.

The position, velocity, and height of both the satellites and the aircraft were numerically propagated, resulting in the state vectors $\boldsymbol{G}_{\mathrm{AC}}$ and $\boldsymbol{G}_{SC}$. The aircraft state vector $\boldsymbol{G}_{\mathrm{AC}}$ was obtained from the open-source database OpenSky [26] using Automatic Dependent Surveillance-Broadcast (ADS-B) data, which included longitude, latitude, altitude, and velocity. Both linear interpolation and a transformation from the longitude, latitude, altitude (LLA) frame to the Earth-centered inertial (ECI) frame were performed. For the satellite state vectors $\boldsymbol{G}_{SC}$, numerical propagation was performed in the ECI frame, using a Runge-Kutta 4 integration and an acceleration model that contained two terms: Earth point gravity acceleration and a J2 perturbation term. The simulation was performed with Tudat [27]. $\boldsymbol{G}$ contained the slant range, looking angles and their rates (elevation, azimuth, and zenith), and the slew rate. It was computed using the relative geometries between $\boldsymbol{G}_{\mathrm{AC}}$ and $\boldsymbol{G}_{SC}$.

Routing was defined as the selection of links between an aircraft and the satellites. This is not the routing of links through the backbone, as has been the case in other studies [14,15]. The acquisition time, the time interval between detection and the start of communication, was fixed at 50 s, based on measurements [16]. The link selection process was modeled using a simplified optimization method, where link duration and overpass elevation were optimized to maximize throughput. At the initiation of each new link at $\boldsymbol{T}_i$, the method filtered satellites based on (1) a positive elevation angle and (2) a positive elevation rate relative to the aircraft. Among the filtered satellites, the one expected to achieve the highest elevation angle during the next overpass was selected. Once the selected satellite's elevation angle dropped below zero, a new link was initiated, repeating the process. This method relied solely on geometric variables. Extending this by incorporating recursion with the throughput metrics will allow a more advanced link selection optimization.

B. Link Level

At this level, the link budget, used to represent the integrated communications performance in terms of gains and losses, was simulated. Then, the atmospheric attenuation process was modeled.

The link budget is defined by Eq. (1). The macro-scale link margin $P_{r,\mathrm{macro}}$ was simulated in step 1 of Fig. 2. The micro-scale channel loss $P_{r,\mathrm{micro}}$ and a power penalty a_{fade} were simulated in step 2, averaged in step 3, and added to $P_{r,\mathrm{macro}}$ in step 4 to obtain the link margin P_r.

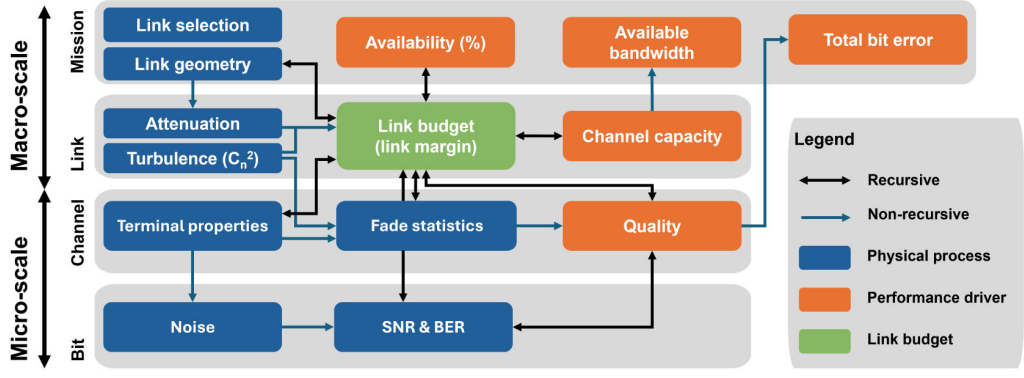

Fig. 3. Diagram of the MMM from Fig. 2 applied to a satellite laser communication service. The physical processes (blue blocks) correspond to Fig. 1.

$$P_r = P_{r,\text{macro}} P_{r,\text{micro}} a_{\text{fade}} = \left[P_T G_T \eta_T L_{fs} L_A \eta_R G_R\right] P_{r,\text{micro}} a_{\text{fade}}. \quad (1)$$

The transmitter gain G_T is defined as the diffraction gain G_{diff} [13] with an added clipping loss T_{clipping} [28] and defocusing effect, commonly applied to size the divergence angle. The total system path loss of each terminal (η_T and η_R) is the product of the coupling losses, splitting losses, and losses owing to transmitter-induced wavefront errors (WFE), as shown in Eq. (2), where η is the system path loss. Splitting losses only applied to the receiver and were used for the acquisition and tracking sensor (ATS), where a reservation of 10% was assumed. For coupling, a single-mode fiber was assumed with a theoretical maximum efficiency of 81%. Finally, a 100 nm root mean square WFE was assumed. $P_{r,\text{micro}}$ is a combination of five micro-scale effects: terminal platform jitter, scintillation, beam wander, angle of arrival (AoA) fluctuations, and turbulence-induced WFE, further explained in Section 4.C.1. a_{fade} is a margin that was added to account for fading effects, as further explained in Section 4.C.2. A threshold of 3 dB is set for the link margin.

$$\eta = \eta_{\text{coupling}} \eta_{\text{splitting}} \eta_{\text{WFE}}. \quad (2)$$

Atmospheric attenuation, caused by the scattering and absorption of molecules and aerosols, was treated as deterministic and directly dependent on the wavelength and link geometry. Considering slant range paths, Beer's law was used to compute the transmission with a varying attenuation coefficient ($\gamma(\lambda, z)$) based on the international standard atmosphere (ISA) model, as described on p. 6 of [29]. An additional attenuation term was added to account for cloud cover. Only cirrus clouds were assumed for the use case in this study, considering an aircraft cruising at 10 km altitude. A static transmission of 0.8 was used, considering small effects above 10 km.

C. Channel Level

At this level, models for the optical beam profile, jitter, and atmospheric turbulence were selected. Then, using the Monte Carlo Power Vector Tool (MCPVT), we simulated the power fluctuations due to the perturbations of the optical signal to obtain $P_{r,\text{micro}}$.

In the propagation channel, a Gaussian beam was assumed with beam waist w_0 defined by a fraction $1/e^2$ of the on-axis intensity I_0, as described in [28]. At the receiving terminal, after the light is received by the aperture, clipping of the telescope results in reshaping of the beam, for which an Airy disk pattern was assumed, as described on p. 22 of [30]. The pointing errors were Rayleigh-distributed [31] and expressed as power fluctuations by projecting the absolute misalignments over the beam intensity profiles. Because the receiving telescope diameter D_r is much smaller than the beam width w_r at the receiver, no variation in power over the telescope aperture was considered. The effective divergence angle in Eq. (3) was computed by taking the diffraction-limited divergence angle $\theta_{\text{div,DL}}$ and adding the clipping loss T_{clipping} and a change in divergence due to defocusing, represented by the M^2 factor.

$$\theta_{\text{div}} = \frac{\theta_{\text{div,DL}}}{\sqrt{T_{\text{clipping}}}} M^2. \quad (3)$$

The turbulence was modeled by simulating the strength of the signal power fluctuations and the temporal power spectrum. The Kolgomorov spectrum was assumed, where the refractive index structure parameter C_n^2 was computed using Hufnagel Valley (HV) [32], as it offers more generality through the inclusion of height variations and wind speed. Although HV is an averaged approximation, it was suitable for this model. The Bufton model was used to determine the wind speed [32], where two velocity terms were added for frequency modeling: the satellite's slew rate ($\omega_{\text{slew}} h$) and the aircraft's transverse velocity ($v_{\text{AC}} \sin(\epsilon)$). The required link geometry for the HV and the wind speed model was directly extracted from $\boldsymbol{G}$, $\boldsymbol{G}_{\text{AC}}$, and $\boldsymbol{G}_{\text{SC}}$.

Five turbulence effects were simulated: (1) short-term (ST) beam wander, (2) WFE, (3) scintillation, (4) long-term (LT) beam wander, and (5) AoA fluctuations. ST beam wander [32] and WFE are assumed to be slowly varying between 1 ms and 1 s. Assuming a tilt-corrected beam, the WFE could be computed using their low-order Zernike modes [8,33]. Assuming a weak turbulence regime for aircraft flying at altitudes well above the Earth's boundary layer, a log-normal distribution was used for scintillation, as computed in [32], where spherical wave simplifications were used for the uplink. Owing to the small apertures, aperture-averaging effects were only considered below 10° elevation, where the turbulence is strong. A Rayleigh distribution was used for the beam wander effects [31]. The AoA variance approximation is described on p. 491 of [32]. The LT beam wander expression from p. 502 in [32] was used.

1. Monte Carlo Power Vector Tool

This tool modeled the stochastic micro-scale processes using a Monte Carlo simulation. For each macro-scale time step $\boldsymbol{T}_i$, the tool generated a distribution of $\boldsymbol{N}$ samples for the seven variables listed in Table 2. These included the turbulence effects and the platform jitter. They were converted into a time series of power vectors, and combined in $P_{r,\text{micro}}(t)$, as shown in Eq. (4). This tool was adopted from [3,5]. The original method considered only beam wander and scintillation, whereas the proposed extension added the three other effects in Table 2. The power vector of the jitter at the transmitter was combined with the beam wander into P_T. The power vector of the jitter at the receiver was combined with the AoA fluctuations into P_R.

$$P_{r,\text{micro}}(t) = P_{\text{scint}} P_T(\theta_T, \theta_{\text{BW}}) P_R(\theta_R, \theta_{\text{AoA}}). \quad (4)$$

Temporal behavior was invoked in the power vectors by filtering the fast Fourier transform (FFT) using low-pass filters. For turbulence, the cutoff frequency ω_t for the filter was determined using the relation on p. 366 of [32]. During cruise flight, the frequency was high owing to the high transverse velocities with respect to the received laser speckles. Platform jitter cutoff frequencies were determined by the mechanical vibration spectrum of an aerial platform, as measured by Airbus. For sufficient resolution, a sampling frequency of 10.0 kHz (0.1 ms) was used. The turbulence frequency ranges between 1–100 ms [5,6].

Table 2. Sampled Variables for the Monte Carlo Simulation[a]

Physical Process	Effect	Symbol	Variable	Distribution
Turbulence	Scintillation	P_{scint}	Norm. power (P/P_0)	Lognormal
	Beam wander	θ_W	Radial angle (rad)	Rayleigh
	Ange of arrival	θ_{AoA}	Radial angle (rad)	Rayleigh
Platform	Jitter (transmitter)	θ_T	X- and Y-component angles (rad)	Rayleigh
	Jitter (receiver)	θ_R	X- and Y-component angles (rad)	Rayleigh

[a]Transmitter and receiver jitter consist of two variables each, representing the X- and Y-component.

2. Fading Statistics

Fades in the received signal provide information regarding quality and temporal behavior. Fading statistics include the mean fade time, number of fades, and fractional fade time. The statistics were numerically computed and were based on P_r and the terminal sensitivity (expressed as the threshold signal power $P_{r,\text{thres}}$). When averaging P_r to the macro-scale, all information regarding the fades is lost. To preserve this information, a buffer a_{fade} was added to the link equation in the form of a loss [34], as defined in Eq. (5). Instead of only accounting for scintillation, we extended the method to the combined signal P_r including all five micro-scale effects defined in Section 4.C.1. P_{min} is the minimum average power required to maintain a certain fractional fade time. First P_{min} was numerically computed for a required fractional fade time of 1%. Then $P_{r,\text{avg}}$ was computed as the average of P_r over $\boldsymbol{N}$ micro-scale time steps for each $\boldsymbol{T}_i$.

$$a_{\text{fade}} = P_{\text{min}}/P_{r,\text{avg}}. \tag{5}$$

D. Bit Level

At this level, models were selected to simulate the optical noise, the detection of the optical signal, and the modulation of the electrical signal, to obtain $\boldsymbol{u}_t^T$. The MMM allows for an additional stochastic simulation at the nanosecond level, in addition to the millisecond level. However, during this study, all processes in this time scale were computed using analytical equations and were therefore simulated with the same frequency as the channel level (0.1 ms). Thus, we assumed that, for each micro-scale time step $\boldsymbol{t}_{i,j}$, all bit processes were identical.

Four noise contributions were considered significant for an optical signal. Assuming a Gaussian distribution, analytical expressions were used for (1) shot noise [35], (2) background noise [7], (3) thermal noise [20], and (4) noise-against-noise beating [35]. In the case of shot noise, this assumption held for large numbers of photons (above 10–20 photons per bit) [20], which was lower than the threshold defined in Table 3. The single-sided power spectral density S_N, used for each noise contribution, is described on p. 84 of [35] and includes the potential excess noise and gain in the case of an amplified signal.

The SNR and BER were simulated as two variables of $\boldsymbol{u}_t^T$. Only direct detection (DD) techniques were considered and included in the model. These are avalanche photo-diode (APD) detection and PIN detection, with and without an optical pre-amplifier [35]. On-off keying (OOK), binary phase shift keying (BPSK), and pulse position modulation (PPM) were used as modulation techniques [20]. A BER threshold of 1.0E-6 was assumed. The sensitivity was defined as the minimum P_r required to achieve the required BER threshold.

5. RESULTS

The results were simulated using a case study. The selected flight route was a civil flight from Oslo to Eneves, for which Data File 1 was used. We used the API from [26] to extract the data from OpenSky. The selected satellite constellation was the transport layer operated by SDA [16] as it is one of the first planned all optical constellations to be operable. Simulated trajectory data of the satellites are found in Dataset 1, Ref. [27]. All trajectories were plotted in Fig. 4(c). Furthermore, two sets of constraints were defined for both aircraft and satellite LCTs, as shown in Table 3. The macro-scale step size $\Delta\boldsymbol{T}$, micro-scale step size $\Delta\boldsymbol{t}$, and micro-scale time interval $\boldsymbol{N}$ were selected using a convergence analysis, where a range of values of these input parameters was used to simulate the performance output. The largest $\Delta\boldsymbol{T}$ and $\Delta\boldsymbol{t}$, and the smallest $\boldsymbol{N}$ were selected while maintaining a stable output.

With our routing model, the trajectories of the aircraft and satellites led to five links during the aircraft's flight, linking with satellites in both planes of the constellation, as shown in Fig. 4(c). Figure 4(b) shows that the five links differed slightly in terms of elevation, mainly owing to the aircraft's position and the Earth's rotation. Figure 5(a) shows an overall availability of approximately 75% with unavailable periods at the tails of each link. We can optimize the availability by decreasing the gray regions, which can be done either by improving acquisition, selecting other links, or improving link quality at low-elevation angles.

The gray regions in Figs. 5(a) and 5(b) correspond to each other. Indeed, the BER increased significantly in the gray region, where the link margin was lower than 3 dB. However, only the BER performance during the communication window, the white region, was relevant. Owing to the power buffer a_{fade}, a too-high fractional fade time resulted in a negative link margin, making it a limiting factor for the availability. Our model provided more insight into the interdependencies of the macro-scale and micro-scale processes. The lower performance during the first and last links corresponded to a rapid increase in error bits, caused by the ascent and descent of the aircraft, as shown in Fig. 4(a). During this period, a longer slant range and stronger turbulence in the lower atmospheric layers resulted in a lower link quality. It should be noted that the assumption of low cloud cover (transmission of 0.8) was based on a cruising

Table 3. LCT System Characteristics and Simulation Parameters Used for the Results[a]

LCT System	Parameter	Symbol	Unit	Value Aircraft	Value Satellite
Optics	Wavelength	λ	nm	1553	1553
	Data rate	D_r	Gbps	2.5	2.5
	Communication channels	-	#	1	1
	Transmitted signal power	P_T	W	20	10
	Aperture diameter	D	mm	80	80
	Effective divergence	θ_{eff}	µrad	24.72	24.72
	Static pointing error (σ)	θ_{stat}	µrad	4.2	3.5
	Dynamic pointing error (σ)	θ_{dyn}	µrad	3.8	3.7
Detection and	Field of view	Ω	ster	1e-8	1e-8
Modulation	Optical bandwidth	B_O	GHz	2.5	2.5
	Electrical bandwidth	B_E	GHz	1.25	1.25
	Modulation scheme	-	-	OOK-NRZ	BPSK
	Detection scheme	-	-	Preamp. & PIN	Preamp. & PIN
	Amplification gain	M_g	-	150	285
	Noise factor	F	-	4	2
Sensitivity	Threshold	BER	-	1.00E-06	1.00E-06
	Threshold	-	dBm	−43.0	−46.31
Simulation	Macro-scale step size	$\Delta \boldsymbol{T}$	s	6	
	Macro-scale time interval	$\boldsymbol{M}$	hr	1.3	
	Micro-scale step size	$\Delta \boldsymbol{t}$	ms	0.1	
	Micro-scale time interval	$\boldsymbol{N}$	s	5	

[a]For each macro-scale evaluation of $\Delta \boldsymbol{T}$, $\boldsymbol{N}/\Delta \boldsymbol{t} = 5/0.0001 = 50{,}000$ micro-scale evaluations are performed.

altitude of 10 km and was not valid for low altitudes, where cloud cover can significantly degrade, or even break, the link. Therefore, the first and last links are less valid.

The link margin P_r was a model variable used to obtain the availability and provided valuable insight into all performance metrics. Figure 6(a) indeed shows that a negative link margin leads to an unavailable link window (gray region). A significant effect of fading was observed in the link budget, especially in the low-elevation regions, where fading resulted in a 24 dB loss at an elevation of 10°. The poor performance with regard to P_r strengthened the insight that we can potentially improve mission performance either by increasing P_r for the current links (e.g., with higher transmission power or with coding/modulation techniques) or by selecting new links using a more advanced routing model.

Considering the link capacity, Fig. 6(b) shows that the potential throughput, defined in Section 2.B, significantly exceeded the actual throughput, based on a fixed data rate of 2.5 Gbps. According to Shannon-Hartley, a higher link margin is available at higher elevation angles. For this reason, hardware supporting a varying data rate can significantly increase the capacity performance, which explains the discrepancy between potential and actual throughput. The potential throughput decreased slightly for each successive link due

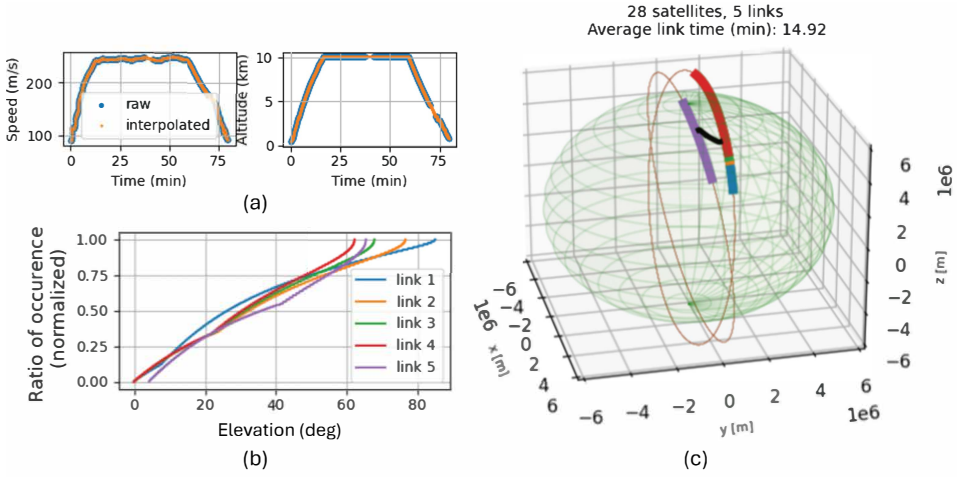

Fig. 4. (a) The altitude and velocity profiles of the aircraft from Oslo to Eneves. See Data File 1 for underlying values (we used the API from [26] to extract the data from OpenSky). (b) Ratio of occurrence of the relative elevation angles between the satellite and aircraft during each link. (c) 3D plot of the aircraft positions $\boldsymbol{G}_{\text{AC}}$ (black), satellite positions $\boldsymbol{G}_{\text{SC}}$ (orange), and the links (highlighted colors). See Dataset 1 for underlying values (simulated with [27]).

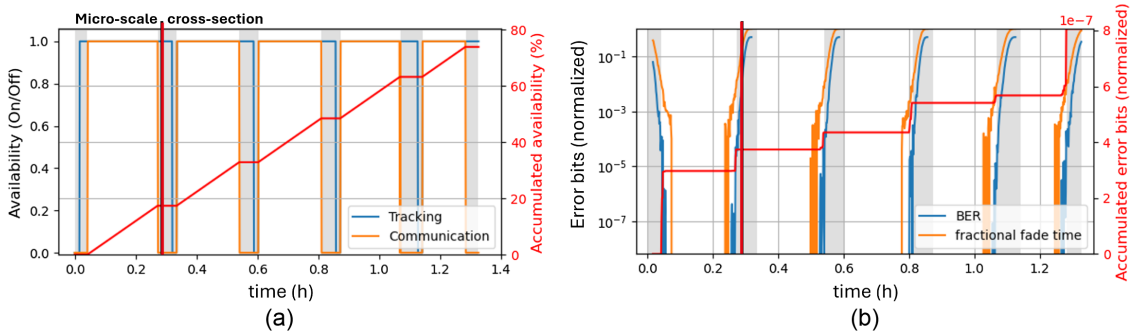

Fig. 5. Time-specific and accumulated values of the availability (a) and quality (b) over all five links throughout the mission. Tracking indicates the initiation of the communication phase, right after acquisition (50 s) is completed. Communication indicates a successful communication link with a positive link margin. The quality is expressed in BER and fractional fade time. The gray regions indicate an unavailable period. Mission level performance is obtained by accumulating the metrics for each $\Delta \boldsymbol{T}$ at the link level (red lines). The accumulated error bits were normalized by dividing them by the total number of transferred bits.

to differences in elevation, as shown in Fig. 4(b). This performance metric provided insight into choosing an optimal fixed data rate or variable data rate, based on the mission type. Telecommunication services may require a constant minimum throughput ensured by a fixed data rate, whereas Earth observation missions may favor a varying data rate that maximizes the throughput per link window.

Figure 7 shows a micro-scale time series of P_r, where the fluctuations were the result of a superposition of frequencies, caused by turbulence (4–5 ms frequency) and mechanical jitter (10–100 ms frequency). This time-series was a cross-section of the macro-scale simulation during the first link at an elevation angle of 10° at 0.26 h, visible in Figs. 6(a) and 6(b) by the red line. The average link margin $P_{r,\mathrm{avg}}$ in Fig. 7 was −34 dBm, corresponding to the blue line at the cross-section in Fig. 6(a). The fractional fade time of this micro-scale time series, defined as the fraction of the signal below the threshold in Fig. 7, was 11%, largely owed to the strong turbulence during the ascent of the aircraft during the first link. To take this large fade into account, the penalty a_{fade} was applied, as the difference between $P_{r,\mathrm{avg}}$ and P_{min}, as explained in Section 4.C.2, leading to a negative link margin of −58 dBm.

A one-to-one validation of the model is difficult given the lack of available experimental data. Instead, all sub-models were individually reproduced and verified using their reference articles. As explained in Section 3, the MMM solely reordered and integrated the sub-models and therefore introduced no physical errors. Also, we compared our service performance with a radio-frequency (RF) broadband constellation, Starlink [17], to perform a sanity check and to indicate the performance potential with respect to current RF technology. Starlink's initial deployment without ISLs achieves an average downlink data rate per satellite of 6.50 Gbps, with a maximum of 19.7 Gbps, as seen in Table 3 of [17]. Our modeled SDA performance in Fig. 6(b) exceeds this slightly. The relatively small difference is owed to Starlink's high single-satellite performance, mainly caused by advanced modulation and coding schemes and steerable multi-beam transceivers, leading to an optical bandwidth of 2 GHz with eight channels of 250 MHz for downlinks. We used one channel without a coding scheme. It should be noted that Starlink currently has ISLs implemented. In addition, we compared the performance of a single link, using measurements by the LOLA mission, an air-to-GEO uplink demonstration [36]. This link showed a BER range of 10^{-3} to 10^{-7} at an elevation around 40° in Fig. 15 of [36]. This agreed with our modeled BER in Fig. 5(b), where the BER range for the first link was 10^{-2} to 10^{-7} between 10° at 0.025 h and 20° at 0.24 h. The higher modeled performance

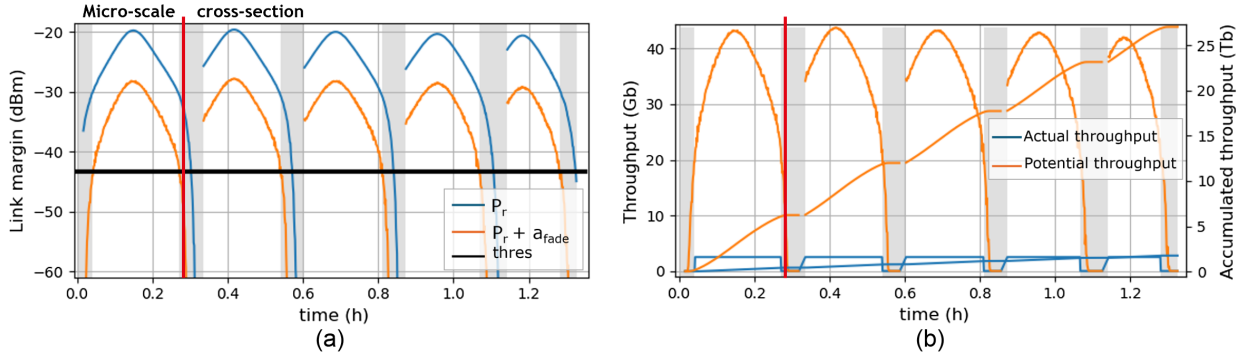

Fig. 6. (a) Average power P_r received by the satellite receivers with the fade buffer a_{fade} and without. The threshold corresponds to the receiver sensitivity for a BER of 1E-6, as seen in Table 3. (b) Time-specific and accumulated link throughput between the satellite and aircraft throughout the mission. Actual throughput was determined by the fixed data rate of 2.5 Gbps. The potential throughput was estimated with the use of the Shannon-Hartley theorem, as explained in Section 2.B. The gray regions indicate an unavailable link window.

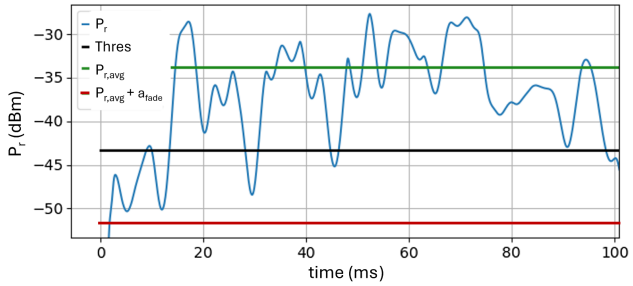

Fig. 7. Micro-scale time series of P_r over 100 ms (1000 evaluations). This is a cross-section of the macro-scale simulation in Figs. 5 and 6 at 10° elevation. $P_{r,\mathrm{avg}}$ is the average link margin and a_{fade} is the power penalty in the case of a fractional fade time of 1%, explained in Section 4.C.2 and plotted in Fig. 6. "Thres" is the threshold signal, indicating the transceiver's sensitivity.

of the SDA can be explained by LOLA's lower altitude of the aircraft (9 km) and longer propagation path to GEO.

Next to the accuracy, the efficiency of the model was estimated by a service simulation time of approximately 6 min using an 8 GB RAM on a normal PC. There were three main efficiency contributors. (1) With the estimated relative position of each satellite with respect to the aircraft, only the links with an elevation higher than 0° were used for modeling the physical layer, reducing the computational cost. (2) Before simulating micro-scale processes, unavailable windows were removed, as seen in Fig. 5(a), leading to a computational cost reduction of approximately 17.1%. Then, (3) simulating a micro-scale time interval of 5 s for every macro-scale time step of 6 s reduced another 16.7%.

6. CONCLUSION

While FSO satellite communication services will prove to be essential for current and future technological developments, no end-to-end model has yet been developed that integrates all physical processes involved in this service. Therefore, we proposed the MMM that integrated and simulated the most dominant processes of the physical layer of an optical satellite communication service end-to-end with availability, quality, and capacity as mission performance drivers. The used method is a modification of the existing multi-scale integration methods HMM and TPCWM. A use case of a 1.3 h aircraft flight route and a polar-orbit satellite constellation was used as an example of how the MMM was applied to an optical air-to-space satellite communication network. This simulation demonstrated successful and efficient modeling of the processes within the physical layer of a satellite communication service. First, linking between these processes on the multiple time scales enabled a better understanding of the interdependencies within the physical layer. Second, insight was obtained into the performance at mission level for each metric separately and combined. This allowed for a trade-off between optimizing the capacity, quality, or availability. Third, it provided insight into the connection of system hardware parameters and the service performance drivers, making it easier to optimize a communication service. Poorly performing links were easily identified, along with their underlying causes.

Acknowledgment. This research is the result of a graduation project at Airbus Netherlands and Delft University of Technology, and there are no costs associated with it. The processing charges are funded by Delft University of Technology.

We thank Jorne Boterman for advice on statistical and numerical modeling. We thank Stijn Mast, Jorne Boterman, Arno de Lange, Lex Meijer, Martijn Visser, and Thomas Dreischer (Airbus Netherlands) for sharing their knowledge of free-space-optics and its applications in space.

Disclosures. The authors declare no conflicts of interest.

Data availability. The data underlying the results presented in this study are available in Data File 1, which contains data from OpenSky extracted with the API from Ref. [26], and Dataset 1, Ref. [27]. The code underlying the model used in this study is available in Code 1, Ref. [37].

REFERENCES

1. H. Kaushal and G. Kaddoum, "Optical communication in space: challenges and mitigation techniques," IEEE Commun. Surv. Tutorials **19**, 57–96 (2017).
2. K. F. Wakker, *Fundamentals of Astrodynamics* (2015).
3. D. Giggenbach, F. Moll, C. Schmidt, *et al.*, "Optical on-off keying data links for low Earth orbit downlink applications," in *Satellite Communications in the 5G Era* (2018).
4. S. Poulenard, M. Crosnier, and A. Rissons, "Ground segment design for broadband geostationary satellite with optical feeder link," J. Opt. Commun. Netw. **7**, 325–336 (2015).
5. D. Giggenbach, A. Shrestha, F. Moll, *et al.*, "Reference power vectors for the optical LEO downlink channel," in *IEEE International Conference on Space Optical Systems and Applications (ICSOS)* (2019).
6. M. Li, M. Wang, X. Kan, *et al.*, "Random vibration analysis in mechanical environment of satellite laser communication terminal telescope," in *2nd International Conference on Artificial Intelligence and Advanced Manufacture (AIAM)* (Institute of Electrical and Electronics Engineers, 2020), pp. 373–376.
7. H. Hemmati, *Deep Space Optical Communications* (Wiley, 2006).
8. R. Parenti, R. J. Sasiela, L. C. Andrews, *et al.*, "Modeling the PDF for the irradiance of an uplink beam in the presence of beam wander," Proc. SPIE **6215**, 621508 (2006).
9. F. Yang, J. Cheng, and T. A. Tsiftsis, "Free-space optical communication with nonzero boresight pointing errors," IEEE Trans. Commun. **62**, 713–725 (2014).
10. H. Ivanov, F. Marzano, E. Leitgeb, *et al.*, "Testbed emulator of satellite-to-ground FSO downlink affected by atmospheric seeing including scintillations and clouds," Electronics **11**, 1102 (2022).
11. M. S. Belen'kii, K. Hughes, and V. Rye, "Free-space laser communication model," Proc. SPIE **5595**, 167–184 (2004).
12. R. Barrios, S. Dimitrov, R. Mata-Calvo, *et al.*, "Link budget assessment for GEO feeder links based on optical technology," Int. J. Satell. Commun. Netw. **39**, 160–177 (2021).
13. D. Giggenbach, M. T. Knopp, and C. Fuchs, "Link budget calculation in optical LEO satellite downlinks with on/off-keying and large signal divergence: a simplified methodology," Int. J. Satell. Commun. Netw. **41**, 460–476 (2023).
14. M. Handley, "Delay is not an option: low latency routing in space," in *ACM Workshop on Hot Topics in Networks (HotNets)* (Association for Computing Machinery, 2018), pp. 85–91.
15. J. Liang, A. Chaudhry, J. Chinneck, *et al.*, "Latency versus transmission power trade-off in free-space optical (FSO) satellite networks with multiple inter-continental connections," IEEE Open J. Commun. Soc. **4**, 3014–3029 (2023).
16. "Optical Communications Terminal (OCT) Standard Version 3.0," Technical report (2021).
17. N. Pachler, I. del Portillo, E. F. Crawley, *et al.*, "An updated comparison of four low Earth orbit satellite constellation systems to provide global broadband," in *IEEE International Conference on Communications Workshops (ICC Workshops)* (2021).
18. "TM synchronization and channel coding" (2023).
19. J. Nielsen, "Nielsen's law of Internet bandwidth" (1998).

20. A. K. Majumdar and J. C. Ricklin, *Free-Space Laser Communications: Principles and Advances* (Springer, 2008).
21. S. Kumar, S. Dalal, and V. Dixit, "The OSI model: overview on the seven layers of computer networks," Int. J. Comput. Sci. Inf. Technol. Res. **2**, 461–466 (2014).
22. G. Frantziskonis, K. Muralidharan, P. Deymier, *et al.*, "Time-parallel multiscale/multiphysics framework," J. Comput. Phys. **228**, 8085–8092 (2009).
23. A. Chatterjee and D. G. Vlachos, "Multiscale spatial Monte Carlo simulations: multigriding, computational singular perturbation, and hierarchical stochastic closures," J. Chem. Phys. **124**, 64110 (2006).
24. A. Abdulle, E. Weinan, B. Engquist, *et al.*, "The heterogeneous multiscale method," Acta Numer. **21**, 1–87 (2012).
25. E. Weinan, *Principles of Multiscale Modeling* (Cambridge University, 2011).
26. X. Olive, "Traffic, a toolbox for processing and analysing air traffic data," J. Open Source Softw. **4**, 1518 (2019).
27. D. Dirkx, J. Garret, G. De Teixeira da Encarnacao, *et al.*, "Positional data of 28 Earth-orbiting (LEO) satellites of the transport layer constellation by SDA, modeled with the use of Tudat, an astronomics toolbox developed by Delft University of Technology," figshare (2010), https://doi.org/10.6084/m9.figshare.28010156.
28. R. Saathof, "AE4880 laser satellite communications II" (2021).
29. D. Vasylyev, W. Vogel, and F. Moll, "Satellite-mediated quantum atmospheric links" (2019).
30. C. Zuo, J. Li, J. Sun, *et al.*, "Transport of intensity equation: a tutorial," Opt. Lasers Eng. **135**, 106187 (2020).
31. M. Toyoshima, T. Jono, K. Nakagawa, *et al.*, "Optimum divergence angle of a Gaussian beam wave in the presence of random jitter in free-space laser communication systems," J. Opt. Soc. Am. A **19**, 567–571 (2002).
32. L. P. Ronald and L. C. Andrews, *Laser Beam Propagation through Random Media* (SPIE, 2005).
33. R. J. Noll, "Zernike polynomials and atmospheric turbulence*," J. Opt. Soc. Am. **66**, 207–211 (1976).
34. D. Giggenbach, "Fading-loss assessment in atmospheric free-space optical communication links with on-off keying," Opt. Eng. **47**, 046001 (2008).
35. P. Gallion, "Basics of incoherent and coherent digital optical communications," in *Undersea Fiber Communication Systems*, 2nd ed., J. Chesnoy, ed. (Academic, 2016), pp. 55–117.
36. V. Chorvalli, L. Le Hors, L. Vaillon, *et al.*, "Optical communications between an aircraft and a GEO relay satellite: design and flight results of the LOLA demonstrator," Proc. SPIE **10566**, 1056619 (2017).
37. W. Helsdingen, "End2end laser SATCOM link model," GitHub (2023) [accessed 14 February 2024], https://github.com/wiegerhelsdingen/lasercom-link-model.